Journal of Materials Science: Materials in Electronics (2019) 30:16015–16029
https://doi.org/10.1007/s10854-019-01972-z

Construction of binary $BiVO_4$/g-C_3N_4 photocatalyst and their photocatalytic performance for reactive blue 19 reduction from aqueous solution coupling with H_2O_2

Yuzhen Li[1,2] · Xiaojin Wang[1] · Lizhen Gao[1,3]

Received: 3 May 2019 / Accepted: 31 July 2019 / Published online: 5 August 2019

Abstract
A highly efficient binary composite consisting of ripple-like sheet g-C_3N_4 doped with paramecium-shape $BiVO_4$ has been successfully fabricated in a mild method and was further characterized by X-ray diffraction, Transmission electron microscopy, Fourier-transform infrared spectroscopy, UV–Vis diffuse reflectance spectrum, and photoluminescence. Their photocatalytic performances were estimated by monitoring the degradation process of reactive blue 19 (RB19) in the aqueous phase under visible light irradiation. The results showed that when the mass ratio of $BiVO_4$ and g-C_3N_4 was 1:5, the binary composite presented the best catalytic activities during the photocatalytic degradation of RB19, and the synthesized composite with H_2O_2 addition could further promote the photocatalytic activities. It is worth mentioning that H_2O_2 acted only as a electron acceptor for accelerating the separation of electron–hole pairs. The trapping experiments showed that $\cdot O_2^-$ was main active species in photocatalytic degradation of RB19. The improving of photocatalytic performance can be put down to the synergistic effect of g-C_3N_4, $BiVO_4$, and H_2O_2 in Z-scheme mechanism, which give rise to enlarge optical absorption range and suppress the recombination of photo-generated charge carrier.

1 Introduction

Synthetic dyes have been widely concerned as pollutants produced from chemical industry in the world since they have long-lasting impacts on marine ecosystems and human health due to its high toxicity, carcinogenicity, complex structure and refractory degradation [1, 2]. Synthetic dyes are being substantially used in plastics, cosmetics, leather, food, pharmaceutical, textile, printing, and dyeing industries. Reactive blue 19 (RB19), also called Remazol Brilliant blue, is a typical stable and resistant anthraquinone reactive dye [3]. This anionic dye may have mutagenicity and toxicity because of the presence of electrophilic vinyl sulfone groups, and more precisely, it has a certain negative effect on human liver, skin and appendix [4, 5].

The removal of synthetic dyes from industrial wastewater generally include physical [6], chemical [7], biological methods [8], or combinations of these three methods [9]. Those treatment technologies for synthetic dyes include activated sludge process, microbiological cultivation, dye-decolorizing peroxidases [10], flocculation, precipitation, filtration, adsorption [11], ultrasonic, microwave, electro-Fenton [12], and photocatalysis [13]. Currently, biological methods have disadvantages of long processing time, expensive equipment, poor-stability, and cumbersome testing [8]. Meanwhile, general adsorption process just transfers hazardous pollutants from aqueous solution to adsorbents rather than completely destroying their structures and degrading them into innocuous small molecules [5]. Additionally, electrochemical oxidations are mostly operated in strong acids or concentrated salt electrolytes, which may increase treatment cost resulting less feasibility to be scaled up in engineering practices [12]. And the traditional Fenton techniques can only achieve high efficiency under high acid conditions (pH 2–3), and ferric ions still remain in the wastewater, complicating the whole process and even causing secondary metal pollution [2]. For this reason, photocatalytic treatment represents an advanced

✉ Yuzhen Li
liyuzhen@tyut.edu.cn; liyuzhen123456@126.com

1 College of Environmental Science and Engineering, Taiyuan University of Technology, 79 Yingze Street, Wanbailin District, Taiyuan 030024, China

2 China Institute for Radiation Protection, 102 Xuefu Street, Xiaodian District, Taiyuan 030006, China

3 School of Mechanical Engineering, University of Western Australia, 35 Stirling Highway, Perth, WA 6009, Australia

oxidation technology of removing organic pollutants thanks to its extremely efficient degradation rate and high mineralization efficiency with CO_2, H_2O, and other minerals as final products. At present, photocatalysts have been developed mainly including metal oxides (TiO_2 [14], ZnO [15]), metal sulfides (CdS [16, 17], ZnS [18]), noble metal semiconductors (BiOX (X = Cl, Br, I) [19], $BiVO_4$ [20], AgCl [21]), and non-metal semiconductors (g-C_3N_4 [22]). However, most of traditional photocatalysts could only absorb UV light and are excited to generate holes to degrade organic pollutants, thus limiting their practical applications [23]. Consequently, in recent years, the synthesis of visible light responsive photocatalysts is one of hot spots in photocatalysis research in order to maximize the utilization of solar energy [24]. Kalikeri et al. [25] have synthesized PANI-TiO_2 nanocomposite by in situ polymerization of aniline along with Degussa P25 (TiO_2) for RB19 degradation. RB-19 dye solution of 50 mg L^{-1} at pH 3 can be completely degraded with catalyst dosage of 1 g L^{-1} in 120 min under visible light irradiation, and the COD removal rate is high to 86%, indicating the dye can be mineralized. Khan et al. [3] found that the S-TiO_2 catalyst could effectively enhance the degradation of RB19 dye through the supportive effect between the photocatalysis and sonolysis. The coupling effect increases the surface area of catalyst, the mass transport between the solution phase and catalyst surface, and the amount of reactive radical species. Although traditional TiO_2 photocatalysts could be modified to achieve the purpose of using the visible light, the traditional approach necessitates extremely acidic conditions, cumbersome operations and expensive equipment.

Fortunately, g-C_3N_4 (graphene-like carbon nitride) could overcome abovementioned difficulties, and it was first reported in 2009 initially as a metal-free conjugated semiconductor photocatalyst for hydrogen production [26]. Since then, it has been receiving more and more attention not only because it has a visible light absorption region of around 470 nm, but also because it has multiple advantages that are non-toxic, low cost, easy to synthesize, soft phase, sp^2-bonded C-N structure, high reduction ability, ideal band gap position, tunable electron band structure, and excellent thermal-chemical stability [27–29]. Nevertheless, similar to the other semiconductor photocatalyst, pure g-C_3N_4 also has some weakness, which is the limited specific surface area, low quantum efficiency, wide band gap energy (~ 2.7 eV) and fast recombination rate of electron hole pairs [30–33], both of which have limited its photocatalytic performance. In order to improve its functions, g-C_3N_4 are often doped with ions/metals/non-metals or combined with other visible-light driven semiconductors of a matched band structure and electron affinity. These composite photocatalysts are mainly developed based upon the coupling effect. Many reports have confirmed that it could improve the separation efficiency of photogenerated carriers, and optimize light capture capacity of g-C_3N_4 to achieve overall enhanced photocatalytic performance [34–36]. Inspired by above studies, many articles have reported that preparation of various visible light-driven photocatalyst nanocomposites were based on g-C_3N_4, moreover, their photocatalytic activities in different photocatalytic reactions were studied, including Mn-doped g-C_3N_4 [37], ZnS/g-C_3N_4 composites [38], Co_3O_4/g-C_3N_4 Z-scheme system [39], Bi_2WO_6/g-C_3N_4 photocatalyst [40], nanosheet-like Bi/α-Bi_2O_3/g-C_3N_4 heterostructure [41], β-Bi_2O_3@g-C_3N_4 core–shell nanocomposite [42] and three-dimensional (3D) ternary graphene-carbon quantum dots/g-C_3N_4 nanosheet (GA-CQDs/CNN) [43].

Of these, there are three different polymorphs of bismuth vanadate ($BiVO_4$), and the monoclinic scheelite (m-s) crystal form has been extensively investigated owing to its narrow band gap energy (~ 2.40 eV) and abundance [44, 45]. Although pure $BiVO_4$ has certain defects including poor specific surface area, high recombination rate of electron and hole pairs, low visible light capture efficiency, and lower quantum yield, some studies have proved that g-C_3N_4 doped with $BiVO_4$ can enhance the visible light catalysis by extending the effective charge carrier lifetime to some extent by effective Z-scheme heterojunction transfer [44, 46]. In order to form a more efficient charge transfer system, H_2O_2 was used as an electron acceptor to inhibit the recombination of photogenerated electron–hole pairs [47, 48].

However, there is little information on the degradation of RB19 by $BiVO_4$/g-C_3N_4 composites coupling with H_2O_2 under visible-light. Therefore, the research objective of this paper was to synthesize $BiVO_4$/g-C_3N_4 composites with a facile wet-impregnation method by doping different content of (m-s) $BiVO_4$ to g-C_3N_4, to investigate the photocatalytic effects of the as-achieved $BiVO_4$/g-C_3N_4 composites with different dosage of H_2O_2 on the removal of reactive blue 19 (RB19) in water solutions under visible-light (λ > 420 nm) irradiation, and to propose a possible Z-scheme mechanism for binary $BiVO_4$/g-C_3N_4 composites and H_2O_2 based on the results of characterization, photocatalytic activity, and radical-trapping experiment.

2 Methodology

2.1 Materials

All chemicals used in the research were analytical grade reagents, and used without further purification. And all solutions are formulated with distilled deionized water (DDI water). Urea (H_2NCONH_2) was purchased from

Tianjin Damao Chemical Reagent Factory (China). Bismuth nitrate ($Bi(NO_3)_3{\cdot}5H_2O$) was procured from Tianjin Kaitong Chemical Reagent Co., Ltd. Methanol (CH_3OH), ethanol absolute (CH_3CH_2OH) and ammonium oxalate ($(NH_4)_2C_2O_4{\cdot}H_2O$) were provided by Tianjin Zhiyuan Chemical Reagent Co., Ltd. Ammonium vanadate (NH_4VO_3) was supplied from Sinopharm Group Chemical Reagent Co., Ltd. Acetic acid 36% (CH_3COOH) was got from Tianjin Guangfu Technology Development Co., Ltd. Ammonia solution ($NH_3{\cdot}H_2O$), hydrochloric acid (HCl) and sodium hydroxide (NaOH) were obtained from Tianjin Sailboat Chemical Reagent Co., Ltd. Hydrogen peroxide 30% (30% H_2O_2) was supplied from Tianjin KeMiou Chemical Reagent Co., Ltd. Tert-butyl alcohol ($(CH_3)_3COH$) was provided from Tianjin Beichen Founder Reagent Factory. Benzoquinone ($C_6H_4O_2$) was purchased from Tianjin Qinghua Jinying Technology Co., Ltd. RB19 was got from Shanghai Macklin Biochemical Co., Ltd. The RB19 stock solution (400 mg L^{-1}) was prepared by adding 0.4 g RB19 powders into 1000 mL DDI water.

2.2 Synthesis of $BiVO_4$/g-C_3N_4 composites

2.2.1 Synthesis of g-C_3N_4

The g-C_3N_4 was prepared according to the method previously described as following [49]: firstly, urea (15 g) was put into an aluminum crucible with a cover under ambient pressure and normal room temperature in air. Following upon it was heated in an electric furnace at a heating rate of 5 °C min^{-1} until the temperature reached 550 °C, subsequently was kept for 4 h in air atmosphere. After cooling down to the room temperature, the pale-yellow g-C_3N_4 products were ground, collected and placed in a desiccator.

2.2.2 Synthesis of $BiVO_4$

Paramecium-shape-like $BiVO_4$ was prepared by hydrothermal treatment in a typical procedure [44], 5 mmol of $Bi(NO_3)_3{\cdot}5H_2O$ was completely dissolved in 10 mL of acetic acid to form a transparent solution by magnetic stirring. Meanwhile, 5 mmol of NH_4VO_3 was added in 60 mL of DDI water and heated to 80 °C to form a clear yellow-green solution. Next, the latter solution was slowly dropped into the former one, and after 20 min ultrasonic treatment and 30 min magnetic stirring, resulting in the formation of an orange-yellow precipitate. Subsequently, the $NH_3{\cdot}H_2O$ was added to the above mixture solution to adjust the pH to 9, after 2 h stirring, and the mixture solution was transferred into a 100 mL Teflon-lined autoclave kept at 140 °C for 20 h. And then the product was washed by DDI water and ethanol to neutral, dried in oven at 50 °C for the whole night. Finally, the $BiVO_4$ powder was obtained after the product was submitted to a calcination treatment at 300 °C for 2 h.

2.2.3 Synthesis of $BiVO_4$/g-C_3N_4

Synthesis of $BiVO_4$/g-C_3N_4 hybrid photocatalyst was performed according to the following procedure [44]: firstly, 1 g of as-prepared g-C_3N_4 was poured into 100 mL of methanol followed by ultrasonic bath for 2 h at room temperature to obtain homogeneous g-C_3N_4 dispersion. Afterwards, a certain amount of $BiVO_4$ was added into the above homogeneous g-C_3N_4 dispersion, and after ultrasonic bath for 1 h, the mixture was stirred in a fume hood for 24 h. After volatilization of the methanol, the resulting product was collected, washed with ethanol and DDI water, and dried at 50 °C for the whole night. At last, the $BiVO_4$/g-C_3N_4 heterojunction was obtained after 2 h calcination at 300 °C. $BiVO_4$/g-C_3N_4 hybrid photocatalysts with different weight ratios of $BiVO_4$ were prepared from 10 to 30 wt% (weight percentage). And the obtained composites were sequentially referred to as xB/CN with x representing the weight percentages of $BiVO_4$ (x was adjusted as 10%, 15%, 20%, 25%, and 30%).

2.3 Characterization

The as-prepared photo-catalysts were characterized in detail as follows: X-ray diffraction (XRD) detected the crystal structures and phase data, which used a LAB XRD-6000 X-ray Diffractometer (40 kV, 30 mA, $\lambda = 0.154$ nm) with a Cu Kα radiation source at a scanning rate of 2° min^{-1} in 2θ ranging from 10° to 80°. Transmission electron microscopy (TEM) was carried out on a JEM-2500SE microscope at 200 kV in order to examine the particle size and morphology of the samples. Fourier-transform infrared spectroscopy (FT-IR) was employed to qualitatively analyze the functional groups and bonds of samples on a Thermo Scientific Nicolet iS10 spectrometer at a frequency range of 4000 ~ 400 cm^{-1} with samples embedded in a KBr pellet. Hitachi U-3900 UV–Vis spectrophotometer was used to measure the light absorption properties of the as-prepared photocatalysts with $BaSO_4$ as a reflectance standard with a scan range of 200 ~ 800 nm. Photoluminescence (PL) was performed on a Shimadzu RF-6000 fluorescence spectrophotometer in air at the normal atmospheric temperature and the excitation wavelength was 380 nm. Its scanning rate was 6000 nm min^{-1} in the 400 ~ 700 nm range, and the bandwidth of excitation and emission was 3 nm.

2.4 Photocatalytic test

The photocatalytic activities of the as-prepared photocatalysts were evaluated by degrading RB19 aqueous solution under visible light irradiation using a 300 W Xe lamp with a UV-cutoff filter (> 420 nm) as the visible light source. Photocatalytic tests were carried out using a discontinuous batch system including a Pyrex reactor filled with 250 mL aqueous suspension containing 20 mg L^{-1} of RB19 and the photocatalyst. In a typical photocatalytic experiment, prior to light irradiation, 250 mg of photocatalysts and 250 mL of RB19 aqueous solution with a concentration of 20 mg L^{-1} were ultrasonicated for 10 min and then stirred in darkness for 40 min in order to reach absorption–desorption equilibrium. Subsequently, 0.25 mL of H_2O_2 was added and meanwhile the light was turned on, then taken a certain volume of reacting solution every 20 min, centrifuged at 10,000 r min^{-1} for 5 min for two times and filtered with 0.45 μm microporous membrane to ensure all the photocatalysts were separated. The concentration of RB19 solution was analyzed at the maximum absorption wavelength 594 nm with a UV-1800PC spectrophotometer (MAPADA, Shanghai, China). The photodegradation efficiency of the RB19 was calculated according to Eq. (1):

$$\eta = \frac{C}{C_0} \tag{1}$$

in which C is the concentration of RB19 for each irradiated time interval at 594 nm, while C_0 is the original concentration.

The photodegradation rate constant of RB19 dye was calculated according to Eq. (2):

$$k_{obs} = -\frac{1}{t} \ln\left(\frac{C}{C_0}\right) \tag{2}$$

where k_{obs} (min^{-1}) is the photodegradation rate constant, C_0 is the RB19 dye concentration after dark adsorption (mg L^{-1}), C is the RB19 dye concentration at irradiation time t (min).

In addition, photocatalytic activities of different photocatalysts, $BiVO_4$/g-C_3N_4 hybrid photocatalysts with different weight ratios of $BiVO_4$, the dosage of the catalyst, the dosage of H_2O_2, the initial pH and the initial concentration of RB19 solution were also researched.

2.5 Active species trapping experiment

To investigate the active species generated in the visible light photocatalytic process of RB19 decomposition, under the same conditions, benzoquinone (BQ, 0.02 g), tert-butyl alcohol (TBA, 0.2 mL) and ammonium oxalate (AO, 0.05 g) were added into RB19 dye solutions as scavengers and utilized for quenching hydroxyl radicals and holes to capture superoxide radicals ($\cdot O_2^-$), hydroxyl radicals ($\cdot$OH), and photo-holes (h^+), respectively.

3 Results and discussion

3.1 Characterization

The phase analysis of the as-prepared photocatalyst was performed using XRD and was shown in Fig. 1. The pure g-C_3N_4 had two obvious characteristic peaks, one feeble peak at 12.98° was indexed as the (100) plane, and the other strong peak at 27.52° was related to the (002) plane, which could be corresponded to the graphitic phase with tri-s-triazine unit (JCPDS No. 87-1526) [48, 50]. The specific peaks of $BiVO_4$ at 18.67°, 18.99°, 28.95°, 30.55°, 34.49°, 35.22°, 39.78°, 42.46°, 45.59°, 46.03°, 46.71°, 47.31°, 50.31°, 53.31°, 58.53° and 59.26° were corresponded to the (110), (011), (121), (040), (200), (002), (211), (051), (231), (132), (240), (042), (202), (161), (321) and (123) crystal plane (JCPDS No. 14-0688), respectively, which could be assigned to monoclinic phase $BiVO_4$ according to the position and intensity of the diffraction peaks [28, 44, 51]. It can be clearly observed from Fig. 1 that the XRD pattern of the binary 20% B/CN composites had the characteristic peaks of g-C_3N_4 at 27.52° and monoclinic phase $BiVO_4$, simultaneously, which indicated that the binary $BiVO_4$/g-C_3N_4 composites had been successfully synthesized, and the crystal phases of g-C_3N_4 and $BiVO_4$ did not significantly change. It means that the binary $BiVO_4$/g-C_3N_4 composite photocatalysts maintained the physical integrity of pure $BiVO_4$ and pure g-C_3N_4.

The morphology and microstructure of the as-prepared pure g-C_3N_4 and binary 20% B/CN samples were observed

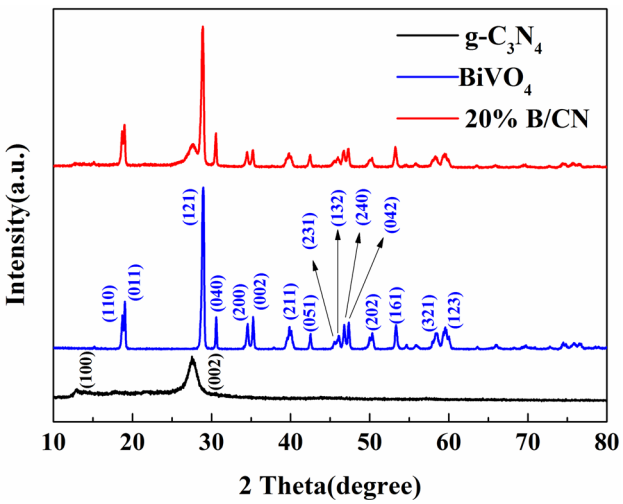

Fig. 1 XRD patterns of g-C_3N_4, $BiVO_4$, 20% B/CN samples

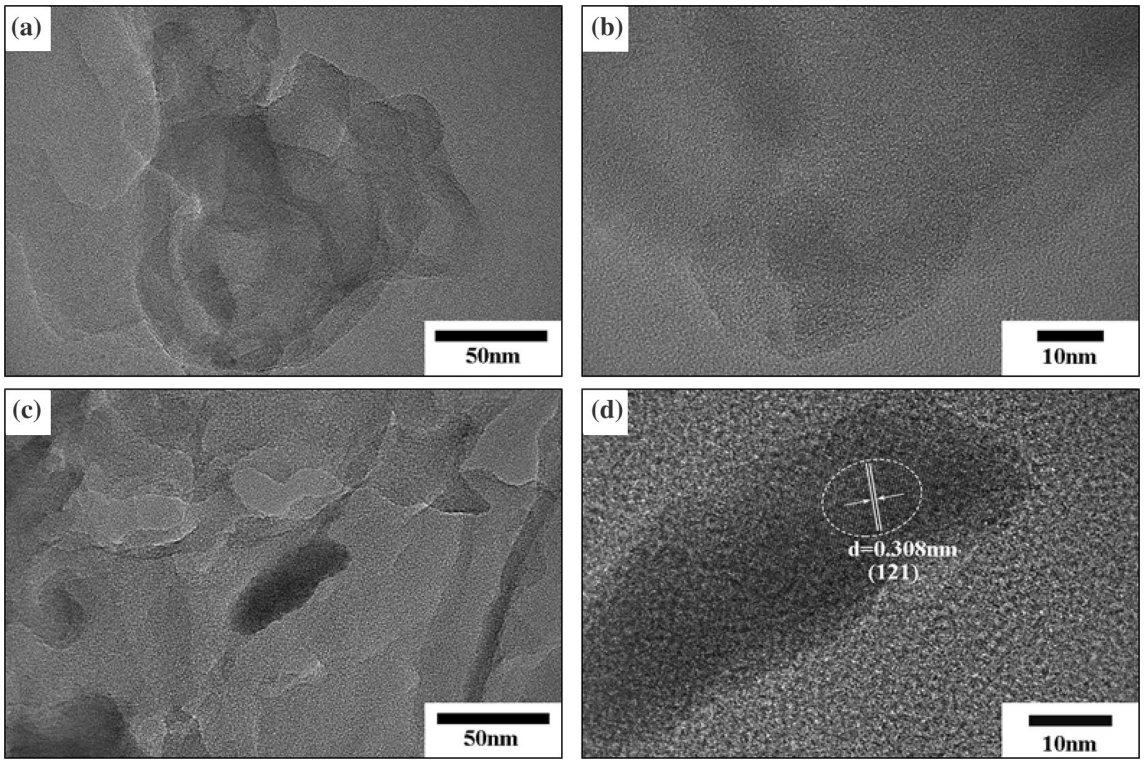

Fig. 2 TEM images of bare g-C_3N_4 **a** scale bar 50 nm, **b** scale bar 10 nm; and the binary 20% B/CN composites, **c** scale bar 50 nm, **d** scale bar 10 nm

by TEM images. As shown in Fig. 2a and b, the pure g-C_3N_4 exhibited a ripple-like sheet structure with some wrinkles. It can be clearly seen from Fig. 2c that nanosheet g-C_3N_4 was embedded with a shape of paramecium-like pure $BiVO_4$. The flexible g-C_3N_4 structures made $BiVO_4$ easily anchored. And $BiVO_4$ were distributed well on the "base" g-C_3N_4 materials. Moreover, the high-magnification TEM image in Fig. 2d shows that lattice spacing of 0.308 nm corresponded to the (121) planes of the monoclinic phase $BiVO_4$ [50, 52].

The FT-IR spectroscopy was used to identify the chemical functional groups of the prepared pure g-C_3N_4 and binary 20% B/CN samples, and the results are presented in Fig. 3. For pure g-C_3N_4, the obvious peaks located at 812 and 880 cm^{-1} could be corresponded to the characteristic bending vibration of s-triazine and triazine units, respectively [22]. The several weak peaks located at 1225, 1320, 1409, and 1568 cm^{-1} were associated with stretching vibrations of the typical aromatic C-N heterocyclic units, and another weak peak at 1641 cm^{-1} was assignable to the C=N stretching vibration mode [53]. The broad bands ranged from 3090 to 3300 cm^{-1} related to N–H and O–H stretching vibrations, which were caused by the residual amino groups and not completely volatilization of H_2O [22]. For 20% B/CN composites, the main characteristic peaks of the pure g-C_3N_4 samples still existed. It can be speculated that the introduction of $BiVO_4$ does not change the initial structure

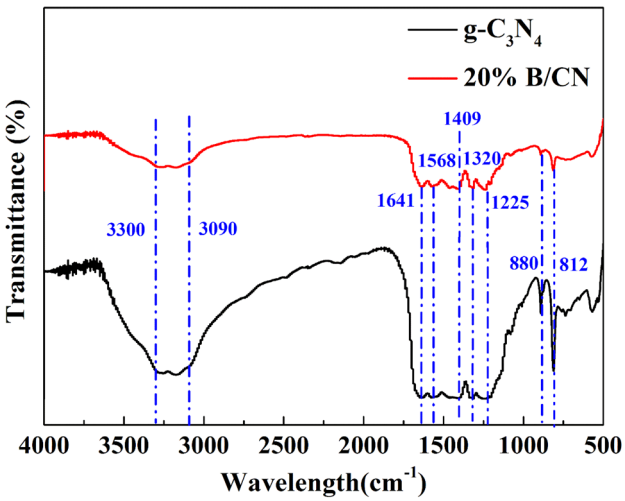

Fig. 3 FT-IR analysis of g-C_3N_4 and 20% B/CN

of the g-C_3N_4. Although the typical peaks of $BiVO_4$ may be too small to be detected, it can be proved that $BiVO_4$ was successfully incorporated into pure g-C_3N_4 by the characterization results of XRD, TEM and UV–Vis diffuse reflectance spectrum (DRS). A similar situation had appeared in a previous literature [27].

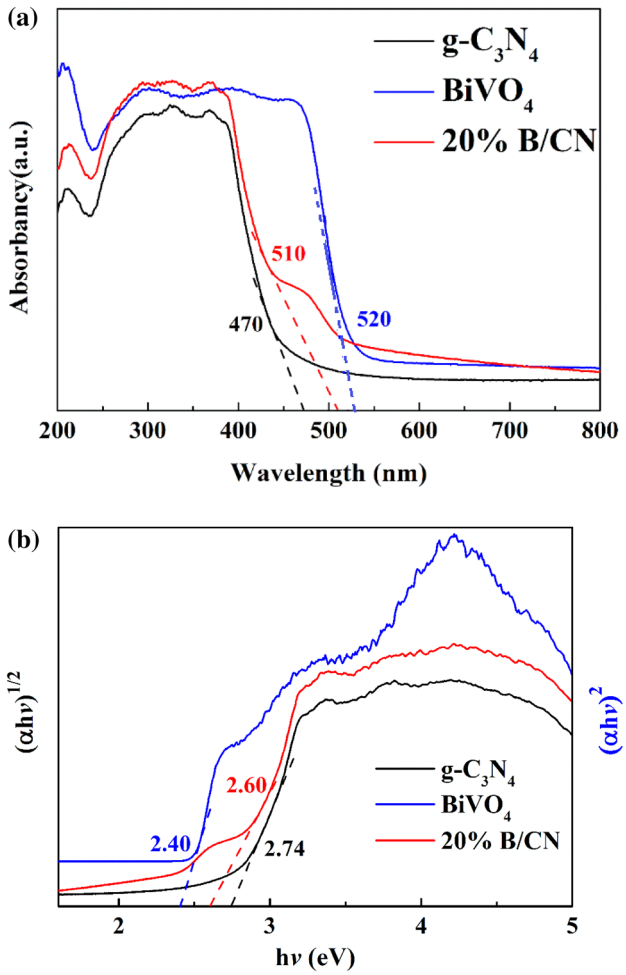

Fig. 4 **a** UV–Vis diffuse reflectance spectrum, **b** the curve is $(\alpha h\nu)^{1/2}$ versus energy ($h\nu$): g-C_3N_4 and 20% B/CN composites, the curve of $(\alpha h\nu)^2$ versus energy ($h\nu$) of $BiVO_4$

In order to investigate the optical properties of the as-prepared samples and further demonstrate their photocatalytic activities under visible light, UV–Vis diffuse reflectance spectrum (DRS) was carried out (Fig. 4). As shown in Fig. 4a, the pure g-C_3N_4 showed a narrow absorption edge at about 470 nm, and the absorption edge of pristine $BiVO_4$ was located at around 520 nm. Both had photonic absorption capability in visible-light region and were basically in accordance with the reported research results [24, 46]. Interestingly, compared to pure g-C_3N_4, binary 20% B/CN photocatalyst exhibited an obvious red shift from 470 nm to 510 nm, while compared with $BiVO_4$, the absorption edge presented slight blue shift. It was notable that the optical absorption intensity of 20% B/CN in UV-light region was higher than those of g-C_3N_4 and $BiVO_4$. This result reveals that doping the wider visible light absorption region of $BiVO_4$ on the g-C_3N_4 with narrow visible light absorption area is beneficial to enhance the optical property of g-C_3N_4. Based on those data, the optical absorption

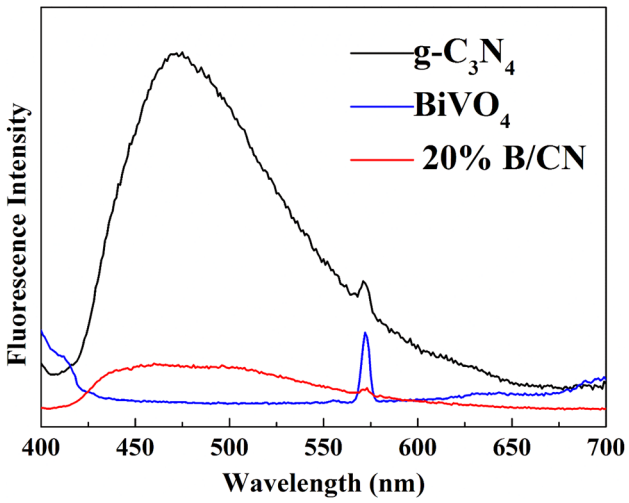

Fig. 5 PL spectra of as-prepared g-C_3N_4, $BiVO_4$ and 20% B/CN excited by 380 nm in air at room temperature

band gap energy (Eg) of the samples could be determined according to Kubelka–Munk function Eq. (3):

$$\alpha h\nu = A\left(h\nu - E_g\right)^{\frac{n}{2}} \tag{3}$$

where α, h, ν, A and E_g represent the absorption coefficient, Planck constant, light frequency, a proportionality constant, and band gap energy, respectively.

The index n depends on the optical transition properties of a semiconductor, n = 1 for a direct-gap semiconductor, and n = 4 for an indirect-gap semiconductor, while the values of n for g-C_3N_4 and $BiVO_4$ are 4 and 1, respectively [52, 54]. The band gaps of the samples are estimated from the plots of $(\alpha h\nu)^{1/2}$ or $(\alpha h\nu)^2$ versus energy ($h\nu$). As shown in Fig. 4b, the band gaps of g-C_3N_4, $BiVO_4$ and binary 20% B/CN photocatalyst are determined to be 2.74, 2.40 and 2.60 eV, respectively. Then, the potentials of conduction band (CB) and valence band (VB) for a semiconductor material can be calculated according to Eqs. (4) and (5):

$$E_{CB} = X - E^e - 0.5E_g \tag{4}$$

$$E_{VB} = E_{CB} + E_g \tag{5}$$

where X is the electronegativity of the semiconductor, which is the geometric mean of the electronegativity of the constituent atoms. The X values for g-C_3N_4 and $BiVO_4$ are 4.67 eV and 6.16 eV, respectively [52]. E^e is the energy of free electrons on the hydrogen scale (4.5 eV/NHE) [52]. Then the CB energy and VB energy of g-C_3N_4 are calculated to be − 1.20 eV/NHE and + 1.54 eV/NHE, whereas they are + 0.46 eV/NHE and + 2.86 eV/NHE for $BiVO_4$, respectively.

The photoluminescence emission spectrum was used to reflect the transition and separation rate of photogenerated

electron–hole pairs. The lower emission peak intensity of the sample means the slower recombination rate of the photoexcited electrons-holes pairs, and then the higher photocatalytic activity of the sample [55]. The PL spectra of pure g-C_3N_4, pure $BiVO_4$ and binary 20% B/CN composite under excitation at 380 nm were shown in Fig. 5. It can be distinctly observed that pure g-C_3N_4 emerged a strong emission peak near 470 nm, which was just right coincided with the visible light absorption edge of the g-C_3N_4 photocatalysts. However, the PL spectra show that the PL emission peak intensity of pure g-C_3N_4 at 470 nm was the highest, pure $BiVO_4$ was the smallest, and 20% B/CN was only a little higher than $BiVO_4$ but much smaller than g-C_3N_4. It indicates that the charge recombination rate of g-C_3N_4 was superior and caused its photocatalytic efficiency to be inferior. In contrast, the charge recombination rate of $BiVO_4$ was much lower, which was expected to improve the photocatalytic efficiency of g-C_3N_4. Compared with g-C_3N_4, the addition of $BiVO_4$ reduced the relative intensity of the PL spectrum due to the formation of a heterojunction between $BiVO_4$ and g-C_3N_4 that facilitated efficient separation of electron–hole pairs. Compared with $BiVO_4$, the PL intensity of the binary 20% B/CN composites increased, which was contrary to the ordinary PL test results and might be due to the formation of Z-scheme electrons-holes transfer between g-C_3N_4 and $BiVO_4$ [56]. In the Z-scheme mechanism, the photogenerated electrons in the CB of $BiVO_4$ recombined with the photogenerated holes in the VB of g-C_3N_4, which caused the reduce in PL intensity compared with that of g-C_3N_4.

3.2 Photocatalytic activity

Figure 6a showed the photocatalytic activity graphs of g-C_3N_4, $BiVO_4$, H_2O_2, 20% B/CN, and 20% B/CN + H_2O_2, and the corresponding concentration changes of RB19 under visible light irradiation. Figure 6b revealed the photodegradation rate constant(k_{obs}) of RB19 degradation in different samples. Figure 6c displayed the UV–Vis spectral changes of RB19 in the dark reaction time and photodegradation process in the interaction of 20% B/CN and H_2O_2. As can be seen in Fig. 6a, when there was only a visible light source added without adding a catalyst, the concentration of RB19 dye did not change, which indicated that RB19 dye was stable in visible-light irradiation and self-photolysis did not occur. When 10 mM H_2O_2 was added as a catalyst, the concentration of RB19 dye remained unchanged. These results revealed that although H_2O_2 was a source of hydroxyl groups, its own oxidizing ability was not strong as expected, and the photocatalytic effect was negligible. It can be seen that the addition of g-C_3N_4, $BiVO_4$ and 20% B/CN as a photocatalyst exhibited the RB19 removal of 69.70%, 9.19%, and 95.79%, respectively, after 120 min visible-light irradiation, and the proportion of dark adsorption was 15.4%,

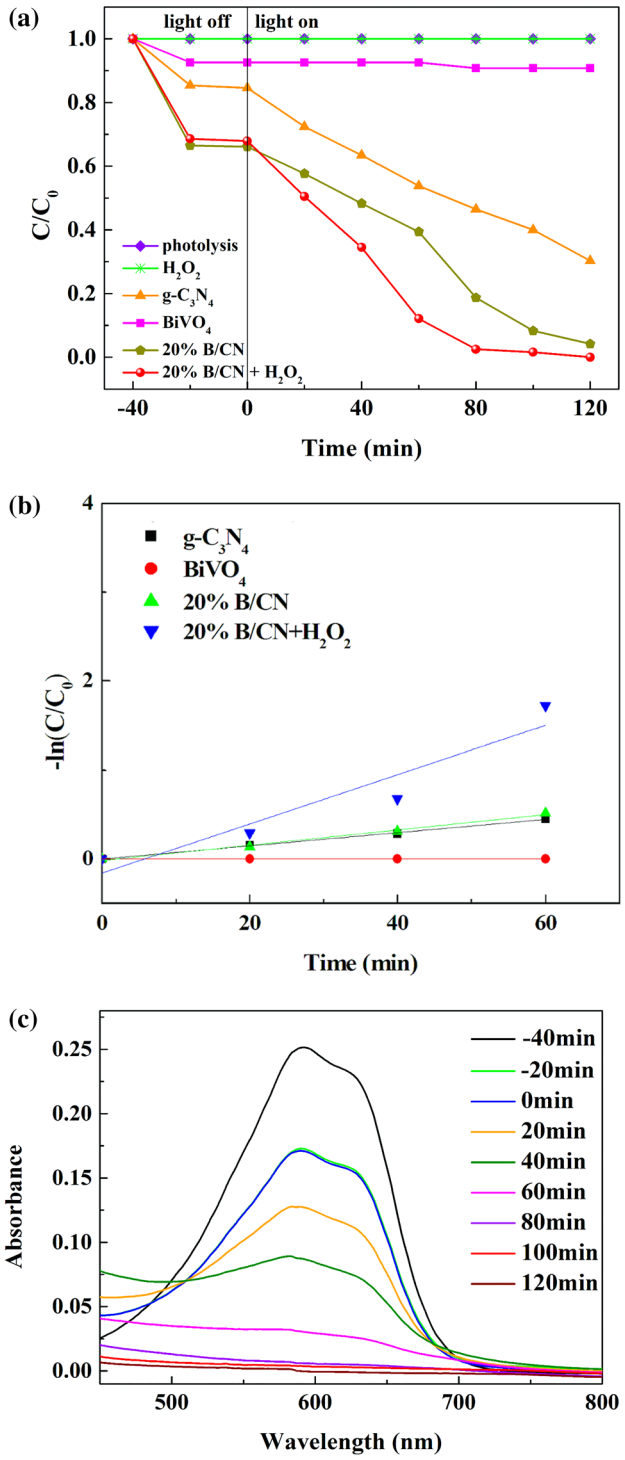

Fig. 6 **a** Photocatalytic activities of different photocatalysts based on the photodegradation of RB19 under visible light. **b** The photodegradation rate constant(k_{obs}) of RB19 degradation in different samples. **c** The UV–Vis absorption spectrum changes for degradation of RB19 over the 20% B/CN + H_2O_2 (C_{RB19} = 20 mg L^{-1}, the dosage of catalyst = 1 g L^{-1}, the dosage of H_2O_2 = 10 mM, pH ~ 7)

7.36% and 33.91%, respectively. The results indicate that after doping a small amount of $BiVO_4$, the pure g-C_3N_4 not only enlarged the specific surface area and increased the adsorption rate, but also remarkably improved the photodegradation efficiency of RB19. Based on the analysis of the UV–Vis absorption spectra, it could be found that the binary 20% B/CN composites broadened the visible light absorption region compared to the pure g-C_3N_4 and narrowed the energy gap, thus reduced the recombination rate of the photogenerated carriers and improved the photocatalytic activity. After further coupling of 20% B/CN and H_2O_2, it increasingly improved the photodegradation of RB19 dye and could degrade 99.98% of RB19 in 120 min. From the Fig. 6b, it was obviously that the photodegradation rate constant(k_{obs}) of RB19 degradation follow in the order: 20% B/CN + H_2O_2 > 20% B/CN > g-C_3N_4 > $BiVO_4$. It can be clearly seen in Fig. 6c that the adsorption equilibrium could be reached after 40-min dark reaction, and the intensity of the absorption peak at 594 nm gradually decreased with the extension of the visible light irradiation time. By combining all the results, it is suggested that the increase in photocatalytic efficiency was due to the electron transfer between 20% B/CN and H_2O_2, rather than the superposition of the respective photocatalytic efficiency.

3.2.1 Effect of $BiVO_4$ doping ratio on g-C_3N_4

Figure 7a and b showed the RB19 concentration changes and the photodegradation rate constant changes of RB19 in 120-min visible-light irradiation over pure g-C_3N_4, pristine $BiVO_4$ and $BiVO_4$/g-C_3N_4 composites with different doping ratio of $BiVO_4$, respectively. It can be seen in Fig. 7a that the photodegradation efficiency of the binary composites was remarkably improved compared to the pure g-C_3N_4 (69.70%) and pristine $BiVO_4$ (9.19%). Especially for the 20% B/CN composite, the degradation efficiency of RB19 reached 95.79%, which was also higher than that of 10% B/CN (78.81%), 15% B/CN (90.36%), 25% B/CN (84.12%), and 30% B/CN (69.86%). And the photodegradation rate constants of RB19 displayed (Fig. 6b) that 0.00856 min^{-1} for g-C_3N_4, 0.00017 min^{-1} for $BiVO_4$, 0.00984 min^{-1} for 10% B/CN, 0.01638 min^{-1} for 15% B/CN, 0.02296 min^{-1} for 20% B/CN, 0.01183 min^{-1} for 25% B/CN, and 0.00664 min^{-1} for 30% B/CN. When the content of $BiVO_4$ is 20%, the photocatalytic rate constant of RB19 reached maximum (0.02296 min^{-1}) within 120-min visible light irradiation, which was 2.68 and 135.06 folds faster than that of pure g-C_3N_4 (0.00856 min^{-1}) and pure $BiVO_4$ (0.00017 min^{-1}), respectively, which is resulting from the morphology and dispersion of 20% B/CN. As can be seen from the Fig. 2c, nanosheet g-C_3N_4 was embedded with a shape of paramecium-like pure $BiVO_4$. And $BiVO_4$were distributed well on the "base" g-C_3N_4 materials. And it can be clearly found

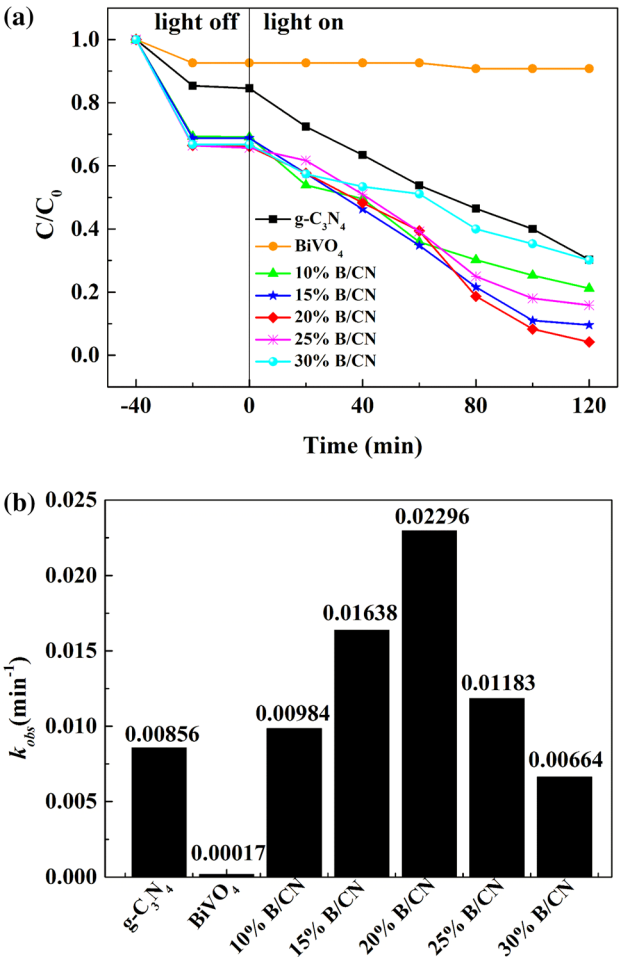

Fig. 7 **a** The photocatalytic efficiency and **b** photoreaction rate constant of RB19 over the g-C_3N_4, $BiVO_4$, 10% B/CN, 15% B/CN, 20% B/CN, 25% B/CN and 30% B/CN (C_{RB19} = 20 mg L^{-1}, the dosage of catalyst = 1 g L^{-1}, pH ~ 7)

from above, along with the amount of $BiVO_4$ increasing, the photocatalytic efficiency of the binary $BiVO_4$/g-C_3N_4 composites did not increase continuously, but it rose first and then dropped off. The phenomenon can be explained by the following two reasons. One reason is that increasing the doping amount of $BiVO_4$ on the g-C_3N_4-based is beneficial to promote the charge transfer and further facilitate the generation of electron–holes pairs. The other reason is that doping excessively $BiVO_4$ on the surface of g-C_3N_4 would prevent effective visible light absorption by g-C_3N_4 and further reduce the quantities of effective heterojunctions in the binary composites, which is detrimental to the charge transfer at the heterojunction interfaces [31, 57].

3.2.2 Effect of 20% B/CN doses for photodegradation RB19

The effects of 20% B/CN composite doses on the photodegradation efficiency and photodegradation rate constant of

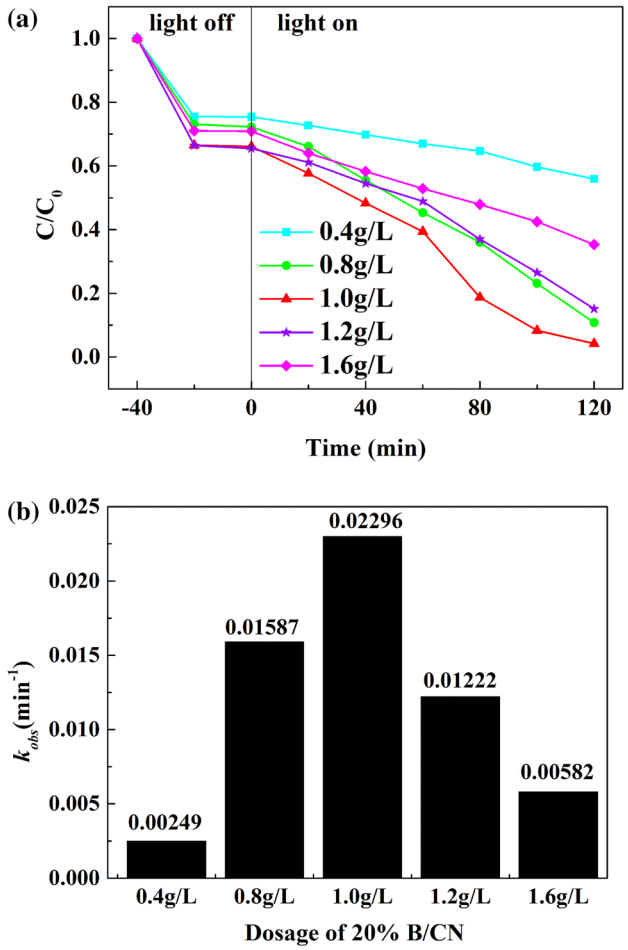

Fig. 8 **a** and **b** Photocatalytic evaluation for RB19 over the different dosage of 20% B/CN (C_{RB19} = 20 mg L^{-1}, pH ~ 7)

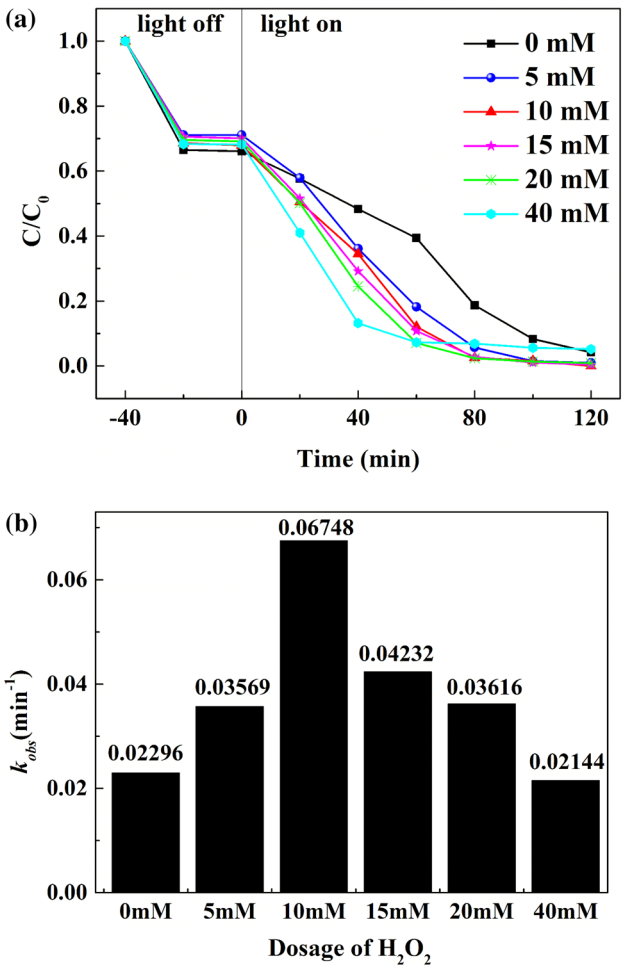

Fig. 9 **a** The photodegradation and **b** photodegradation rate constant of RB19 over the different dosage of H_2O_2 (C_{RB19} = 20 mg L^{-1}, the dosage of 20% B/CN = 1 g L^{-1}, pH ~ 7)

RB19 were presented in Fig. 8. It can be seen that with the increasing of 20% B/CN photocatalysts doses from 0.4 to 1.0 g L^{-1}, the photodegradation efficiency of RB19 increased from 44.09 to 95.79%, the photodegradation rate constant increased from 0.00249 to 0.02296 min^{-1}. When the amount of photocatalysts was larger than 1.0 g L^{-1}, it would bring inhibitory effect to the photodegradation process, and then both the photodegradation efficiency and the photodegradation rate constant exhibited a downward trend. As the dosage of 20% B/CN composite increased from 1.0 to 1.6 g L^{-1}, its photocatalytic activities dropped from 95.79 to 64.72%. It can be concluded that the optimal dosage of 20% B/CN photocatalysts was 1 g L^{-1} in the research. There are two reasons accounting for this situation. On the one hand, as the amount of photocatalyst went up, the binary 20% B/CN composite provided the increase of the active sites for the photodegradation of RB19, and then the photocatalytic performance was sharply boosted. On the other hand, when the amount of the photocatalyst exceeded the optimum value, it would increase the turbidity of the reaction solution resulting in affecting the transmittance of visible light, reducing the visible light absorption rate and the generation of electron–hole pairs on the surface of the binary 20% B/CN composite, and finally decreasing the photocatalytic efficiency [46].

3.2.3 Effect of H_2O_2 on the photodegradation of RB19

To assess the effect of H_2O_2 on the photodegradation of RB19 and further determine the optimal dosage of H_2O_2, experiments were conducted by varying H_2O_2 dosage from 0 to 40 mM, and the results are presented in Fig. 9. After 120-min visible light irradiation, when the H_2O_2 dose was 0, 5, 10, 15, 20, and 40 mM, the photodegradation of RB19 was 95.79%, 99.02%, 99.98%, 99.56%, 99.10%, and 94.80% (Fig. 9a), respectively, and the photodegradation rate constant of RB19 was 0.02296, 0.03569, 0.06748, 0.04232, 0.03616, and 0.02144 min^{-1} (Fig. 9b), respectively. The results mentioned above demonstrated that the photocatalytic process of the prepared 20% B/CN composite after coupling

with H_2O_2 was better than that without H_2O_2. Meanwhile, it is proved that as the amount of H_2O_2 increased, the photocatalytic activities would keep growing and reached the highest at the H_2O_2 dose of 10 mM, and further increasing the doses of H_2O_2 would lead to the decrease. Therefore, it can be concluded that the optimal dosage of H_2O_2 was 10 mM in the study. Similar conclusions have been obtained in the previous two literatures, but both studies set the optimum H_2O_2 concentration as 100 mg L^{-1}. The photocatalytic efficiency of RB19 increased at lower H_2O_2 concentrations possibly because the direct photolysis of H_2O_2 generated radicals, and at higher H_2O_2 concentrations, the increase in photocatalytic efficiency could be attributed to its role as an electronic sacrificial agent, excessive H_2O_2 will react with ·OH to form a much weaker oxidant (·HO_2), and ·HO_2 also has the effect of consuming ·OH [47, 48]. In this study, H_2O_2 itself did not undergo photolysis under visible light (in Fig. 5a), which might be due to the difference in recalcitrance properties of RB19. Therefore, it can be concluded that even a small amount of H_2O_2 also can capture photogenerated electrons, promote photocurrent transfer rate, and improve photodegradation efficiency.

3.2.4 Effect of the initial pH of RB19 on the 20% B/CN and H_2O_2

Considering that pH value is also an important parameter affecting the degradation efficiency of organic pollutants, the experiments were carried out using different initial pH values (pH 3, 5, 7, 9 and 11) of RB19 solution, and the experimental results were demonstrated in Fig. 10. The effect of the initial pH on the amount of dark adsorption can be seen from Fig. 10a. It has been determined that the pH of RB19 stock solution was about 7, and decreasing the pH value to less than 7 or increasing the pH value to higher than 7 would increase the amount of dark adsorption. And the increase in the dark adsorption capacity of acidic pH was stronger than that of alkaline pH. Especially at pH 3, the adsorption amount could reach more than 90%. Because the charges on the surface of the photocatalysts was positive under acidic conditions, they could easily combine with the negative charges on the surface of RB19 dyes by electrostatic attraction, which was beneficial to the adsorption of RB19 dyes on the photocatalysts [25]. It is puzzling that the increase in adsorption efficiency did not cause the increase in the photodegradation of RB19. When the initial pH was 3, 5, 7, 9 and 11, the photodegradation ratio of RB19 were 98.81%, 99.86%, 99.98%, 99.31% and 97.59% within 120-min visible light irradiation, respectively, and the final degradation efficiency had no significant difference. However, after removing the influence of the dark reaction, the difference in photodegradation rate constant was still obvious (Fig. 10b). In this regard, the photocatalytic efficiency was

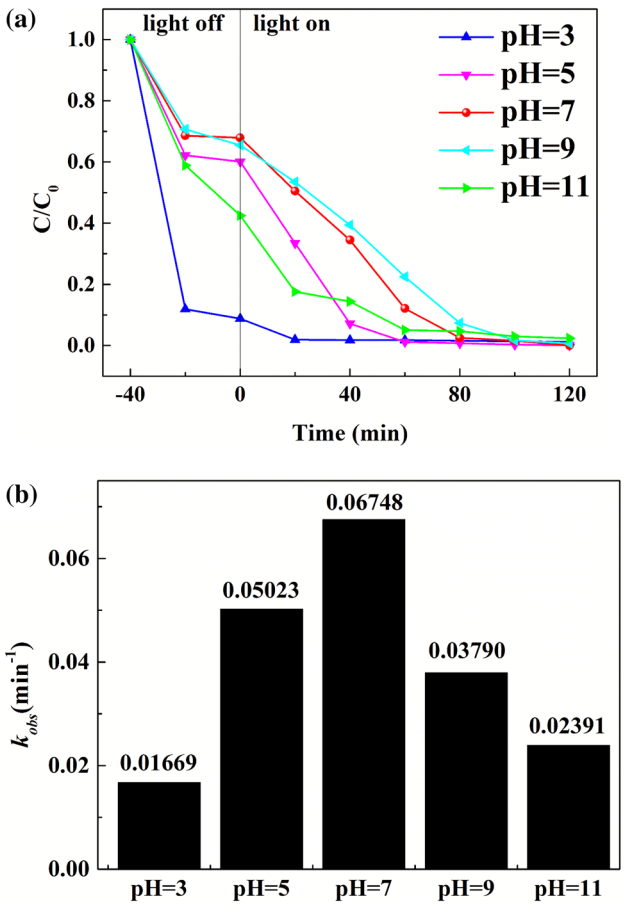

Fig. 10 **a** The photocatalytic performance and **b** photodegradation rate constant of RB19 over the different initial pH (C_{RB19} = 20 mg L^{-1}, the dosage of 20% B/CN = 1 g L^{-1}, the dosage of H_2O_2 = 10 mM)

still the highest at pH 7. The results disagreed with the conclusions obtained in the previous literature [25]. Their works revealed that the lower the pH, the higher the degradation rate of RB19, and the optimum pH was 3. The reason for the difference may be that too much RB19 dyes were adsorbed on the surface of the catalysts, affecting the transmittance of the visible light, and thus impacting its photocatalytic efficiency. However, this study did not elaborate the amount of adsorption of the catalyst.

3.2.5 Effect of RB19 concentrations on the 20% B/CN and H_2O_2

Another major influencing factor for the photocatalytic activity of the photocatalysts was the initial concentration of RB19 dye. Figure 11 showed the effects of different initial concentration of RB19 on photocatalytic degradation. As is demonstrated in Fig. 11, when the initial concentration of RB19 increased from 10 to 60 mg L^{-1}, the dark adsorption amount and photocatalytic degradation

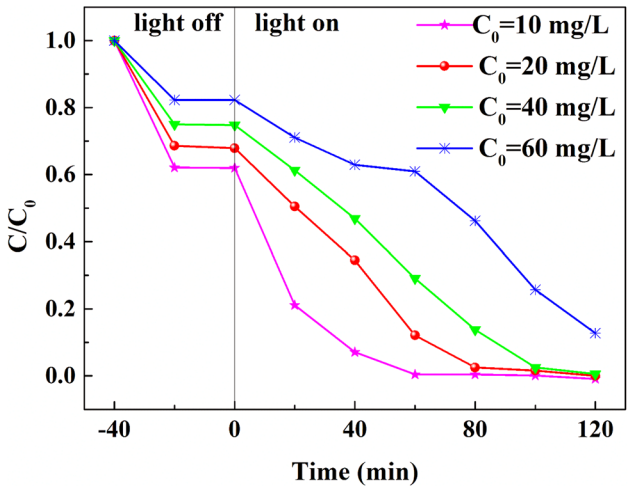

Fig. 11 Comparison of the photodegradation activity over the different initial concentration of RB19 in the same photoreaction condition (the dosage of 20% B/CN = 1 g L^{-1}, the dosage of H_2O_2 = 10 mM, pH ~ 7)

rate decreased in turn. In other words, compared with other concentrations, the 10 mg L^{-1} RB19 solution had the highest dark adsorption capacity and the highest photocatalytic degradation rate. At the same time, it can be found that the photodegradation rate of 10 mg L^{-1} RB19 was faster in the first 60 min, and tended to be gentle after 60 min. Specifically, the photodegradation rate of 10 mg L^{-1} RB19 was 99.55% at 60 min. And RB19 of 10 mg L^{-1} completely degraded at 120 min. For 20 mg L^{-1} RB19, it was degraded faster in the first 80-min photo reaction, and the degradation began to slow down after 80 min irradiation. The photodegradation rates of 20 mg L^{-1} RB19 were 97.50% and 99.98% at 80 min and 120 min, respectively. When higher concentrations were mentioned, for 40 mg L^{-1} RB19 dye, its photodegradation tended to be flat after 100 min, for 60 mg L^{-1} RB19 dye, it did not reach a flat trend within 120 min. Moreover, the photodegradation rates of 40 mg L^{-1} RB19 were 97.50% and 99.36% in 100 min and 120 min, respectively. For 60 mg L^{-1} RB19, its photocatalytic degradation ratio was 87.21% under 120 min visible light irradiation. According to the above experimental results, it can be observed that the photocatalytic reaction was inhibited at a higher initial RB19 dye concentration. When an appropriate amount of RB19 dye was adsorbed on the surface of the binary $BiVO_4$/g-C_3N_4 composites, it would firstly consume photoexcited electron–hole pairs on the surface of the photocatalysts, which also inhibited the recombination and promoted to separate. When the initial concentration of RB19 dye was too high, the turbidity of the solution would increase, the transmittance of visible light would decrease, and the separation rate of

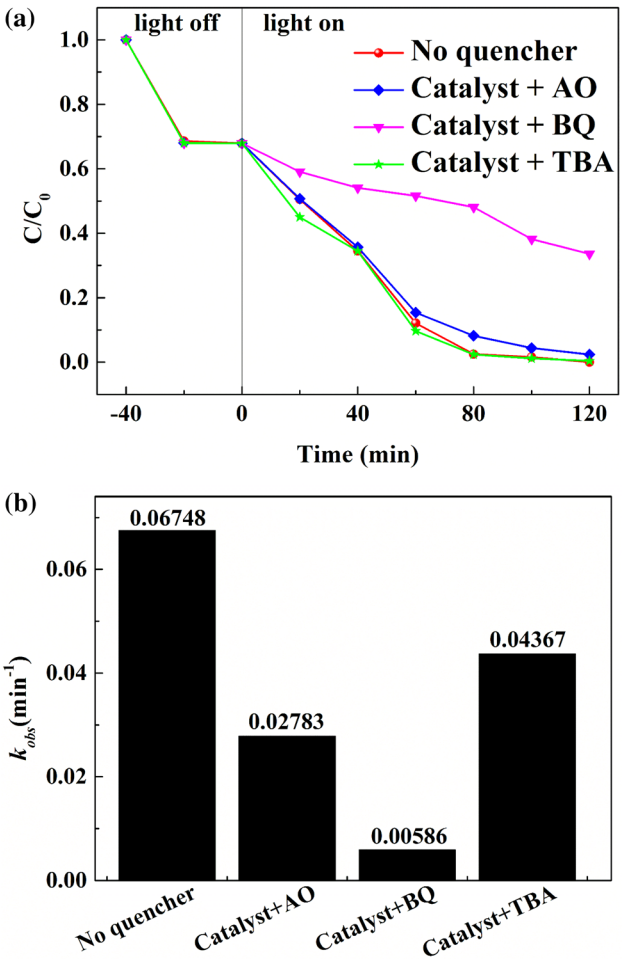

Fig. 12 **a** and **b** The photocatalytic degradation of RB19 with various scavengers over the 20% B/CN photocatalysts (the dosage of 20% B/CN = 1 g L^{-1}, the dosage of H_2O_2 = 10 mM, pH ~ 7)

photogenerated electron-hole pairs in the catalyst would reduce, which ultimately caused the decrease in photocatalytic activities of RB19 dye [46].

3.3 Photocatalytic mechanism

In order to ascertain the active species in the degradation process, some sacrificial agents, such as tert-butyl alcohol (TBA), ammonium oxalate (AO) and 1,4-benzoquinone (BQ), were used as the hydroxyl radical (·OH) scavenger, hole (h^+) scavenger, and superoxide radical ($\cdot O_2^-$) scavenger, respectively. The radical-trapping photocatalytic experimental results are presented in Fig. 12. It can be seen from Fig. 12a that the addition of AO of 0.05 g as a hole scavenger added to the solution had a slight inhibitory effect on the photodegradation process of RB19, and the photocatalytic degradation efficiency of RB19 decreased from 99.98% to 97.59%, indicating that a few of the holes were involved in the degradation of RB19. When BQ of 0.02 g was added

under the same conditions, the photocatalytic degradation efficiency of RB19 changed greatly and suddenly dropped to 66.36% (Fig. 12a), suggesting that the $\cdot O_2^-$ pathways played a crucial role in the process of RB19 degradation. While TBA of 0.2 mL was added, the degradation efficiency hardly changed (99.64%), indicating the absence of ·OH radical species. It can be seen from Fig. 12b that the photodegradation rate constant was 0.06748 min^{-1} when no quencher was added in, and decreased to 0.02783, 0.00586, and 0.04376 min^{-1} after adding AO, BQ, and TBA, respectively. The above results indicate that the $\cdot O_2^-$ radicals were the major active species in the photocatalytic process of RB19 by the system consisted of binary $BiVO_4$/g-C_3N_4 composites and H_2O_2, and the h^+ and ·OH participated in the reactions but their effects are minimal, in which the effect of ·OH was weaker than h^+.

Based on the radical-trapping experimental results mentioned above, a possible Z-scheme mechanism of the prepared binary $BiVO_4$/g-C_3N_4 composite for photodegradation of RB19 by the addition of H_2O_2 was proposed and illustrated in Fig. 13. In the previous study, the reason for forming a Z-scheme transmission mechanism between g-C_3N_4 and $BiVO_4$ instead of the traditional heterojunction was described at some length [50]. What is additionally stated here is that in conventional heterojunctions, when electrons and holes migrated to lower energy levels, both the reduction capability of the electrons and oxidation capability of the holes reduced [35]. However, the Z-scheme transmission mechanism retains the reducing and oxidizing power of electrons and holes to the greatest extent.

It is well known that both $BiVO_4$ and g-C_3N_4 can be easily excited to generate photo-electrons (e^-) and photo-holes (h^+) on the conduction band (CB) and valence band (VB) under visible light irradiation, respectively. The CB and VB for g-C_3N_4 are − 1.20 and + 1.54 eV/NHE, whereas they are + 0.46 and + 2.86 eV/NHE for $BiVO_4$, respectively. In addition, the visible-light optical band gap energies for g-C_3N_4 and $BiVO_4$ are about 2.74 and 2.40 eV, respectively. Firstly, under the excitation of visible light, photoelectrons are transited from the VB of g-C_3N_4 to its CB, and then react with O_2 on the catalyst surface to form peroxyl radicals ($\cdot O_2^-$) owing to that the CB energy of g-C_3N_4 (− 1.20 eV/NHE) is more negative than standard redox potentials $O_2/\cdot O_2^-$ (− 0.33 eV/NHE). Meantime, the photogenerated electrons in the CB of $BiVO_4$ transfer to the VB of g-C_3N_4 due to the electrons migration to this position compared to the VB position of $BiVO_4$, the distance is shorter, and the energy consumed is less. The electrons in the CB position of $BiVO_4$ have occupied the VB of g-C_3N_4, so that the electrons in the CB position of g-C_3N_4 can not be recombined back to its VB position, more and more electrons accumulate on the CB of g-C_3N_4, and finally react with O_2 to generate more $\cdot O_2^-$ to directly degrade RB19. Moreover, the VB energy of g-C_3N_4 (+ 1.54 eV/NHE) is lower than that of ·OH/H_2O (+ 1.99 eV/NHE) and ·OH/OH^- (+ 2.40 eV/NHE), so its photo-holes can not react with H_2O or OH^- to give OH and may directly react with the RB19 dyes. However, most of holes on VB of g-C_3N_4 are occupied by electrons from the CB of $BiVO_4$, so the degradation of RB19 is weak. Meanwhile, a small part of the holes accumulated on VB of $BiVO_4$ will degrade RB19 dyes immediately, and the other part will be oxidized into ·OH owing to that its VB position (+ 2.86 eV/NHE) is more positive than that of ·OH/H_2O (+ 1.99 eV/NHE) and ·OH/OH^- (+ 2.40 eV/NHE). A portion of ·OH radicals used for degrading RB19 dyes and others will further react to generate H_2O_2, $HO_2\cdot$ and O_2. Here, the

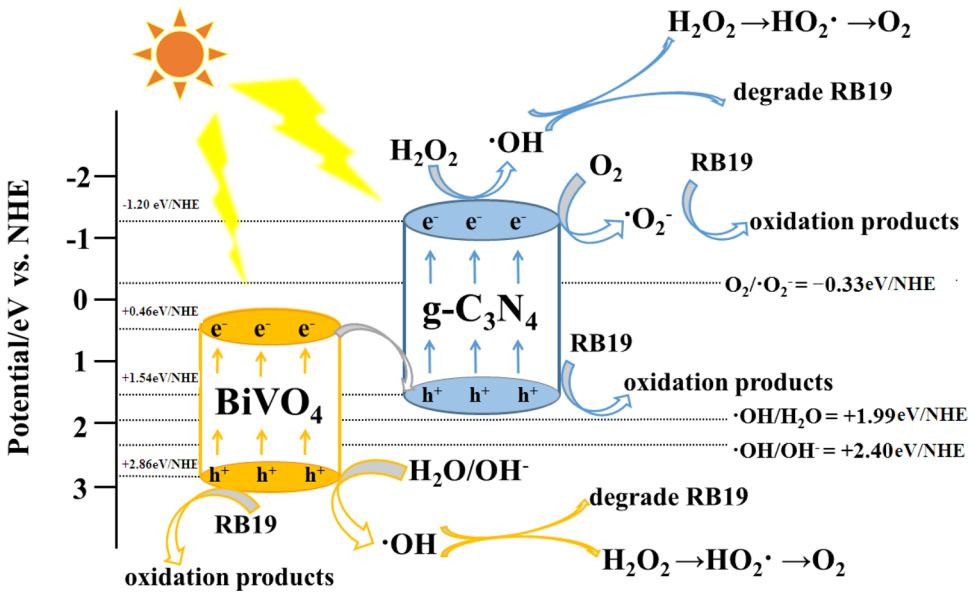

Fig. 13 The schematic of the novel Z-scheme transmission mechanism between g-C_3N_4 and $BiVO_4$ with adding H_2O_2

O_2 continues to be used for the reduction of electrons on the CB of g-C_3N_4, generating $\cdot O_2^-$ to degrade RB19 dyes. When H_2O_2 is added to the photocatalytic reaction system as a photo-electrons capture agent, it could capture photogenerated electrons on the CB of g-C_3N_4 and react with them to form ·OH. The role of the ·OH radicals here is the same as above. All these processes could be described by the following equations (Eqs. (6)–(16)):

$$\text{photocatalysts} + h\nu \rightarrow \text{photocatalysts}(e_{CB}^- + h_{VB}^+) \quad (6)$$

$$e_{CB}^- + O_2 \rightarrow \cdot O_2^- \quad (7)$$

$$O_2^- + RB19 \rightarrow \text{oxidation products} \quad (8)$$

$$h_{VB}^+ + RB19 \rightarrow \text{oxidation products} \quad (9)$$

$$h_{VB}^+ + OH^- \rightarrow \cdot OH \quad (10)$$

$$h_{VB}^+ + H_2O \rightarrow \cdot OH + H^+ \quad (11)$$

$$OH + RB19 \rightarrow \text{oxidation products} \quad (12)$$

$$\cdot OH + \cdot OH \rightarrow H_2O_2 \quad (13)$$

$$H_2O_2 + \cdot OH \rightarrow HO_2 \cdot + H_2O \quad (14)$$

$$HO_2 \cdot + \cdot OH \rightarrow O_2 + H_2O \quad (15)$$

$$H_2O_2 + e_{CB}^- \rightarrow \cdot OH + OH^- \quad (16)$$

The conclusions which is agreement with the Sect. 3.2.4. It can be seen from the Eq. (11) that the higher the concentration of H^+, the smaller the amount of ·OH produced, and the lower the degradation efficiency of the photocatalytic reaction. Similarly, from Eq. (16), the higher the concentration of OH^-, the higher the extent of inhibition of the reaction between H_2O_2 and photoinduced electron (e^-), the less the amount of ·OH produced, and the slower the rate of photodegradation. At the same time, since the amount of ·OH produced is not much, the effect of changing pH on their degradation rate is relatively weak.

4 Conclusion

In summary, a binary photocatalyst was successfully fabricated by loading different ratios of paramecium-shape $BiVO_4$ on the pure g-C_3N_4 ripple-like sheet. The photocatalytic experimental results showed that the 20% B/CN composite without H_2O_2 addition could realize the degradation rate of RB19 of up to 95.79% in a time span of 120 min, and the 20% B/CN composite plus 10 mM H_2O_2, could lift the degradation rate of RB19 to 99.98%. The former and the latter had photodegradation rate of 0.02296 min^{-1} and 0.06748 min^{-1}, which was 2.68 and 7.88 folds of that by pure g-C_3N_4 (0.00856 min^{-1}), respectively. In the novel Z-scheme transmission mechanism composed of binary 20% B/CN composite and H_2O_2, the active species that played a major role in photocatalytic degradation of RB19 are superoxide radicals ($\cdot O_2^-$). The g-C_3N_4 based nanomaterials have excellent photocatalytic performance with low price in degrading organic pollutants such as RB19 and will have more prospective practical application of photocatalysis.

Acknowledgements This work was supported by the Shanxi Provincial Key Research and Development Plan (general) Social Development Project (201703D321009-5).

References

1. M. Bilal, T. Rasheed, H.M.N. Iqbal, C.L. Li, H. Wang, H.B. Hu, W. Wang, X.H. Zhang, Photocatalytic degradation, toxicological assessment and degradation pathway of C.I. Reactive blue 19 dye. Chem. Eng. Res. Des. **129**, 384–390 (2018)
2. Z.J. Huang, P.X. Wu, B.N. Gong, S.S. Yang, H.L. Li, Z. Zhu, L.H. Cui, Preservation of glutamic acid-iron chelate into montmorillonite to efficiently degrade reactive blue 19 in a Fenton system under sunlight irradiation at neutral pH. Appl. Surf. Sci. **370**, 209–217 (2016)
3. M.A.N. Khan, M. Siddique, F. Wahid, R. Khan, Removal of reactive blue 19 dye by sono, photo and sonophotocatalytic oxidation using visible light. Ultrason. Sonochem. **26**, 370–377 (2015)
4. M. Kostic, M. Radović, N. Velinov, S. Najdanović, D. Bojić, A. Hurt, A. Bojić, Synthesis of mesoporous triple-metal nanosorbent from layered double hydroxide as an efficient new sorbent for removal of dye from water and wastewater. Ecotoxicol. Environ. Saf. **159**, 332–341 (2018)
5. I. Morosanu, C. Teodosiu, A. Coroaba, C. Paduraru, Sequencing batch biosorption of micropollutants from aqueous effluents by rapeseed waste: experimental assessment and statistical modelling. J. Environ. Manag. **230**, 110–118 (2019)
6. L. Liu, R. Wang, J. Yu, L.J. Hu, Z.G. Wang, Y.M. Fan, Adsorption of reactive blue 19 from aqueous solution by chitin nanofiber-/nanowhisker-based hydrogels. RSC Adv. **8**, 15804–15812 (2018)
7. V. Mahmoodi, A. Ahmadpour, T.R. Bastami, M.T.H. Mosavian, PVP assisted synthesis of high efficient BiOI/graphene oxide nanohybrid and its photocatalytic performance in degradation of organic dye pollutants. Sol. Energy **176**, 483–495 (2018)
8. M. Bilal, H.M.N. Iqbal, H. Hu, W. Wang, X. Zhang, Enhanced bio-catalytic performance and dye degradation potential of chitosan-encapsulated horseradish peroxidase in a packed bed reactor system. Sci. Total Environ. **575**, 1352–1360 (2017)
9. C.R. Holkar, H. Arora, D. Halder, D.V. Pinjari, Biodegradation of reactive blue 19 with simultaneous electricity generation by the newly isolated electrogenic *Klebsiella* sp. C NCIM 5546 bacterium in a microbial fuel cell. Int. Biodeterior. Biodegrad. **133**, 194–201 (2018)
10. L.L. Li, H. Yuan, F. Liao, B. He, S.Q. Gao, G.B. Wen, X. Tan, Y.W. Lin, Rational design of artificial dye-decolorizing peroxidases using myoglobin by engineering Tyr/Trp in the heme center. Dalton Trans. **46**, 11230–11238 (2017)
11. A. Banaei, S. Samadi, S. Karimi, H. Vojoudi, E. Pourbasheer, A. Badiei, Synthesis of silica gel modified with 2,2′-(hexane-1,6-diylbis(oxy)) dibenzaldehyde as a new adsorbent for the removal of reactive yellow 84 and reactive blue 19 dyes from aqueous solutions: equilibrium and thermodynamic studies. Powder Technol. **319**, 60–70 (2017)

12. W. Zhou, Y.N. Ding, J.H. Gao, K.K. Kou, Y. Wang, X.X. Meng, S.H. Wu, Y.K. Qin, Green electrochemical modification of RVC foam electrode and improved H_2O_2 electrogeneration by applying pulsed current for pollutant removal. Environ. Sci. Pollut. Res. **25**, 6015–6025 (2018)
13. D. Maučec, A. Šuligoj, A. Ristić, G. Dražić, A. Pintar, N.N. Tušar, Titania versus zinc oxide nanoparticles on mesoporous silica supports as photocatalysts for removal of dyes from wastewater at neutral pH. Catal. Today **310**, 32–41 (2018)
14. R.R. Hao, G.H. Wang, C.J. Jiang, H. Tang, Q.C. Xu, In situ hydrothermal synthesis of g-C_3N_4/TiO_2 heterojunction photocatalysts with high specific surface area for Rhodamine B degradation. Appl. Surf. Sci. **411**, 400–410 (2017)
15. S.W. Duo, R.F. Zhong, Z. Liu, J. Wang, T.Z. Liu, C.L. Huang, H.S. Wu, One-step hydrothermal synthesis of ZnO microflowers and their composition-/hollow nanorod-dependent wettability and photocatalytic property. J. Phys. Chem. Solids **120**, 20–33 (2018)
16. Y. Wu, H. Wang, W.G. Tu, S.Y. Wu, Y. Liu, Y.Z. Tan, H.J. Luo, X.Z. Yuan, J.W. Chew, Petal-like CdS nanostructures coated with exfoliated sulfur-doped carbon nitride via chemically activated chain termination for enhanced visible-light–driven photocatalytic water purification and H_2 generation. Appl. Catal. B: Environ. **229**, 181–191 (2018)
17. Z.W. Chen, C. Feng, W.B. Li, Z.Y. Sun, J. Hou, X.B. Li, L.K. Xu, M.X. Sun, Y.Y. Bu, Enhanced visible-light-driven photocatalytic activities of 0D/1D heterojunction carbon quantum dot modified CdS nanowires. Chin. J. Catal. **39**, 841–848 (2018)
18. Q.B. Wei, M.L. Yin, Y. Yao, Synthesis of sphere-like ZnS architectures via a solvothermal method and their visible-light catalytic properties. J. Mater. Sci.: Mater. Electron. **28**, 17827–17832 (2017)
19. H.F. Cheng, B.B. Huang, Y. Dai, Engineering BiOX (X = Cl, Br, I) nanostructures for highly efficient photocatalytic applications. Nanoscale **6**, 2009–2026 (2014)
20. L.Y. Zhang, Z.X. Dai, G.H. Zheng, Z.F. Yao, J.J. Mu, Superior visible light photocatalytic performance of reticular $BiVO_4$ synthesized via a modified sol–gel method. RSC Adv. **8**, 10654–10664 (2018)
21. B. Rodriguez-Cabo, I. Rodriguez-Palmeiro, R. Corchero, R. Rodil, E. Rodil, A. Arce, A. Soto, Photocatalytic degradation of methyl orange, methylene blue and rhodamine B with AgCl nanocatalyst synthesised from its bulk material in the ionic liquid $[P_{6\,6\,6\,14}]Cl$. Water Sci. Technol. **75**, 128–140 (2017)
22. L. Tian, J.Y. Li, F. Liang, J.K. Wang, S.S. Li, H.J. Zhang, S.W. Zhang, Molten salt synthesis of tetragonal carbon nitride hollow tubes and their application for removal of pollutants from wastewater. Appl. Catal. B: Environ. **225**, 307–313 (2018)
23. Z. Wei, J.S. Hu, K.J. Zhu, W.Q. Wei, X.G. Ma, Y.F. Zhu, Self-assembled polymer phenylethnylcopper nanowires for photoelectrochemical and photocatalytic performance under visible light. Appl. Catal. B: Environ. **226**, 616–623 (2018)
24. Y. Li, X.Y. Xiao, Z.H. Ye, Facile fabrication of tetragonal scheelite (t-s) $BiVO_4$/g-C_3N_4 composites with enhanced photocatalytic performance. Ceram. Int. **44**, 7067–7076 (2018)
25. S. Kalikeri, N. Kamath, D.J. Gadgil, V. Shetty Kodialbail, Visible light-induced photocatalytic degradation of reactive blue-19 over highly efficient polyaniline-TiO_2 nanocomposite: a comparative study with solar and UV photocatalysis. Environ. Sci. Pollut. Res. **25**, 3731–3744 (2018)
26. X.C. Wang, K. Maeda, A. Thomas, K. Takanabe, G. Xin, J.M. Carlsson, K. Domen, M. Antonietti, A metal-free polymeric photocatalyst for hydrogen production from water under visible light. Nat. Mater. **8**, 76–80 (2009)
27. R. Wang, X.Y. Kong, W.T. Zhang, W.X. Zhu, L.J. Huang, J. Wang, X. Zhang, X.N. Liu, N. Hu, Y.R. Suo, J.L. Wang, Mechanism insight into rapid photocatalytic disinfection of Salmonella based on vanadate QDs-interspersed g-C_3N_4 heterostructures. Appl. Catal. B: Environ. **225**, 228–237 (2018)
28. R.Z. Sun, Q.M. Shi, M. Zhang, L.H. Xie, J.S. Chen, X.M. Yang, M.X. Chen, W.R. Zhao, Enhanced photocatalytic oxidation of toluene with a coral-like direct Z-scheme $BiVO_4$/g-C_3N_4 photocatalyst. J. Alloys Compd. **714**, 619–626 (2017)
29. X.W. Shi, M. Fujitsuka, Z.Z. Lou, P. Zhang, T. Majima, In situ nitrogen-doped hollow-TiO_2/g-C_3N_4 composite photocatalysts with efficient charge separation boosting water reduction under visible light. J. Mater. Chem. A **5**, 9671–9681 (2017)
30. Y.Z. Liu, H.Y. Zhang, J. Ke, J.Q. Zhang, W.J. Tian, X.Y. Xu, X.G. Duan, H.Q. Sun, M.O. Tade, S.B. Wang, 0D (MoS_2)/2D (g-C_3N_4) heterojunctions in Z-scheme for enhanced photocatalytic and electrochemical hydrogen evolution. Appl. Catal. B: Environ. **228**, 64–74 (2018)
31. Y. Wu, H. Wang, W.G. Tu, Y. Liu, Y.Z. Tan, X.Z. Yuan, J.W. Chew, Quasi-polymeric construction of stable perovskite-type $LaFeO_3$/g-C_3N_4 heterostructured photocatalyst for improved Z-scheme photocatalytic activity via solid p-n heterojunction interfacial effect. J. Hazard. Mater. **347**, 412–422 (2018)
32. H. Zhao, H.Z. Zhang, G.W. Cui, Y.M. Dong, G.L. Wang, P.P. Jiang, X.M. Wu, N. Zhao, A photochemical synthesis route to typical transition metal sulfides as highly efficient cocatalyst for hydrogen evolution: from the case of NiS/g-C_3N_4. Appl. Catal. B: Environ. **225**, 284–290 (2018)
33. S.A. Ansari, M.H. Cho, Simple and large scale construction of MoS_2-g-C_3N_4 heterostructures using mechanochemistry for high performance electrochemical supercapacitor and visible light photocatalytic applications. Sci. Rep. **7**, 43055 (2017)
34. S. Gholizadeh Khasevani, N. Mohaghegh, M.R. Gholami, Kinetic study of navy blue photocatalytic degradation over Ag_3PO_4/$BiPO_4$@MIL-88B(Fe)@g-C_3N_4 core@shell nanocomposite under visible light irradiation. New J. Chem. **41**, 10390–10396 (2017)
35. L.Y. Lu, G.H. Wang, M. Zou, J. Wang, J. Li, Effects of calcining temperature on formation of hierarchical TiO_2/g-C_3N_4 hybrids as an effective Z-scheme heterojunction photocatalyst. Appl. Surf. Sci. **441**, 1012–1023 (2018)
36. B.Y. Liang, D.H. Han, C.H. Sun, W.X. Zhang, Q. Qin, Synthesis of SnO/g-C_3N_4 visible light driven photocatalysts via grinding assisted ultrasonic route. Ceram. Int. **44**, 7315–7318 (2018)
37. J.C. Wang, C.X. Cui, Y. Li, L. Liu, Y.P. Zhang, W. Shi, Porous Mn doped g-C_3N_4 photocatalysts for enhanced synergetic degradation under visible-light illumination. J. Hazard. Mater. **339**, 43–53 (2017)
38. J. Wang, P. Guo, Q.S. Guo, P.G. Jönsson, Z. Zhao, Fabrication of novel g-C_3N_4/nanocage ZnS composites with enhanced photocatalytic activities under visible light irradiation. Cryst. Eng. Commun. **16**, 4485–4492 (2014)
39. H.J. Wu, C.M. Li, H.N. Che, H. Hu, W. Hu, C.B. Liu, J.Z. Ai, H.J. Dong, Decoration of mesoporous Co_3O_4 nanospheres assembled by monocrystal nanodots on g-C_3N_4 to construct Z-scheme system for improving photocatalytic performance. Appl. Surf. Sci. **440**, 308–319 (2018)
40. Y.Y. Zhao, X.H. Liang, Y.B. Wang, H.X. Shi, E.Z. Liu, J. Fan, X.Y. Hu, Degradation and removal of Ceftriaxone sodium in aquatic environment with Bi_2WO_6/g-C_3N_4 photocatalyst. J. Colloid Interface Sci. **523**, 7–17 (2018)
41. D.D. Chen, S.X. Wu, J.Z. Fang, S.Y. Lu, G.Y. Zhou, W.H. Feng, F. Yang, Y. Chen, Z.Q. Fang, A nanosheet-like α-Bi_2O_3/g-C_3N_4 heterostructure modified by plasmonic metallic Bi and oxygen vacancies with high photodegradation activity of organic pollutants. Sep. Purif. Technol. **193**, 232–241 (2018)
42. Y.Z. Hong, C.S. Li, B.X. Yin, D. Li, Z.Y. Zhang, B.D. Mao, W.Q. Fan, W. Gu, W.D. Shi, Promoting visible-light-induced

photocatalytic degradation of tetracycline by an efficient and stable beta-Bi_2O_3@g-C_3N_4 core/shell nanocomposite. Chem. Eng. J. **338**, 137–146 (2018)
43. H.J. He, L.H. Huang, Z.J. Zhong, S.Z. Tan, Constructing three-dimensional porous graphene-carbon quantum dots/g-C_3N_4 nanosheet aerogel metal-free photocatalyst with enhanced photocatalytic activity. Appl. Surf. Sci. **441**, 285–294 (2018)
44. F. Chen, Q. Yang, Y.L. Wang, J.W. Zhao, D.B. Wang, X.M. Li, Z. Guo, H. Wang, Y.C. Deng, C.G. Niu, G.M. Zeng, Novel ternary heterojunction photocatalyst of Ag nanoparticles and g-C_3N_4 nanosheets co-modified $BiVO_4$ for wider spectrum visible-light photocatalytic degradation of refractory pollutant. Appl. Catal. B: Environ. **205**, 133–147 (2017)
45. F.Q. Zhou, J.C. Fan, Q.J. Xu, Y.L. Min, $BiVO_4$ nanowires decorated with CdS nanoparticles as Z-scheme photocatalyst with enhanced H_2 generation. Appl. Catal. B: Environ. **201**, 77–83 (2017)
46. Y.C. Deng, L. Tang, C.Y. Feng, G.M. Zeng, J.J. Wang, Y.Y. Zhou, Y.N. Liu, B. Peng, H.P. Feng, Construction of plasmonic Ag modified phosphorous-doped ultrathin g-C_3N_4 nanosheets/$BiVO_4$ photocatalyst with enhanced visible-near-infrared response ability for ciprofloxacin degradation. J. Hazard. Mater. **344**, 758–769 (2018)
47. A.C. Affam, M. Chaudhuri, Degradation of pesticides chlorpyrifos, cypermethrin and chlorothalonil in aqueous solution by TiO_2 photocatalysis. J. Environ. Manag. **130**, 160–165 (2013)
48. X.S. Rong, F.X. Qiu, J. Rong, X.L. Zhu, J. Yan, D.Y. Yang, Enhanced visible light photocatalytic activity of W-doped porous g-C_3N_4 and effect of H_2O_2. Mater. Lett. **164**, 127–131 (2016)
49. S.W. Hu, L.W. Yang, Y. Tian, X.L. Wei, J.W. Ding, J.X. Zhong, P.K. Chu, Simultaneous nanostructure and heterojunction engineering of graphitic carbon nitride via in situ Ag doping for enhanced photoelectrochemical activity. Appl. Catal. B: Environ. **163**, 611–622 (2015)
50. Q.G. Meng, H.Q. Lv, M.Z. Yuan, Z. Chen, Z.H. Chen, X. Wang, In situ hydrothermal construction of direct solid-state nano-Z-scheme $BiVO_4$/pyridine-doped g-C_3N_4 photocatalyst with efficient visible-light-induced photocatalytic degradation of phenol and dyes. ACS Omega **2**, 2728–2739 (2017)
51. Z.Q. He, Y.Q. Shi, C. Gao, L. Wen, J.M. Chen, S. Song, BiOCl/$BiVO_4$ p–n heterojunction with enhanced photocatalytic activity under visible-light irradiation. J. Phys. Chem. C **118**, 389–398 (2013)
52. N. Tian, H.W. Huang, Y. He, Y.X. Guo, T.R. Zhang, Y.H. Zhang, Mediator-free direct Z-scheme photocatalytic system: $BiVO_4$/g-C_3N_4 organic-inorganic hybrid photocatalyst with highly efficient visible-light-induced photocatalytic activity. Dalton Trans. **44**, 4297–4307 (2015)
53. L.Q. Jing, Y.G. Xu, Z.G. Chen, M.Q. He, M. Xie, J. Liu, H. Xu, S.Q. Huang, H.M. Li, Different morphologies of SnS_2 supported on 2D g-C_3N_4 for excellent and stable visible light photocatalytic hydrogen generation. ACS Sustain. Chem. Eng. **6**, 5132–5141 (2018)
54. D.L. Jiang, P. Xiao, L.Q. Shao, D. Li, M. Chen, RGO-promoted all-solid-state g-C_3N_4/$BiVO_4$ Z-scheme heterostructure with enhanced photocatalytic activity toward the degradation of antibiotics. Ind. Eng. Chem. Res. **56**, 8823–8832 (2017)
55. Z.S. Zhang, M. Wang, W.Q. Cui, H. Sui, Synthesis and characterization of a core–shell $BiVO_4$@g-C_3N_4 photo-catalyst with enhanced photocatalytic activity under visible light irradiation. RSC Adv. **7**, 8167–8177 (2017)
56. S.P. Wan, M. Ou, W. Cai, S.L. Zhang, Q. Zhong, Preparation, characterization, and mechanistic analysis of $BiVO_4$/$CaIn_2S_4$ hybrids that photocatalyze NO removal under visible light. J. Phys. Chem. Solids **122**, 239–245 (2018)
57. Y.J. Si, Y.J. Zhang, L.H. Lu, S. Zhang, Y. Chen, J.H. Liu, H.Y. Jin, S.E. Hou, K. Dai, W.G. Song, Boosting visible light photocatalytic hydrogen evolution of graphitic carbon nitride via enhancing it interfacial redox activity with cobalt/nitrogen doped tubular graphitic carbon. Appl. Catal. B: Environ. **225**, 512–518 (2018)